

High Impedance Arc Fault Detection Based on the Harmonic Randomness and Waveform Distortion in the Distribution System

Mingjie Wei , Student Member, IEEE, Fang Shi , Hengxu Zhang , Member, IEEE, Zongshuai Jin , Vladimir Terzija , Fellow, IEEE, Jian Zhou, and Hailong Bao

Abstract—High impedance arc faults (HIAFs) happening in the medium-voltage distribution system may result in damages to devices and human security. However, great difficulties exist in identifying these faults due to the much weaker features and the varieties when grounded with different surfaces. This paper presents an integrated algorithm to detect the HIAFs with high-resolution waveform data provided by distribution-level PMUs deployed in the system. An improved arc model is proposed, which can continuously imitate the randomness and intermittence during the “unstable arcing period” of arc faults. The integrated algorithm consists of two branches. First, the variations of HIAFs during unstable arcing period are identified with the unified harmonic energy and global randomness index, which can unify the scales of harmonic content in different fault situations and enlarge the disparities from non-fault conditions. Then, the waveform distortions of HIAFs during the stable arcing period are identified with discrete wavelet transform to extract the detailed distribution characteristics. The reliability and security of the proposed algorithm are verified with numerical simulations and field tests in a 10-kV distribution system.

Index Terms—The distribution system, medium voltage, high impedance arc fault, randomness, waveform distortion, PMU.

I. INTRODUCTION

HIGH impedance arc faults (HIAFs) usually happen in the medium-voltage (MV) distribution system when the energized conductor poorly contacts the high-impedance grounding surfaces with continuous luminosity and electricity discharge [1], [2], which could result in great damages to system operations and human security. However, the detection of HIAFs is still

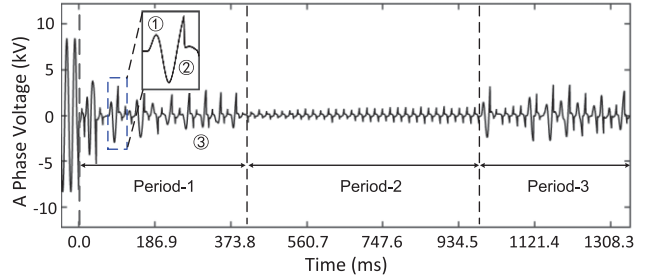


Fig. 1. Voltage waveform of field arc fault in a 10-kV distribution system.

unreliable due to the lower fault current, which is far less from the short circuit faults. Statistically, only about 20% of them can be detected by conventional relays [3].

A grounded arc always begins with a transient process referred to as ‘unstable arcing period’ (Period 1 and 3 in Fig. 1), whose duration varies from at least milliseconds to more than tens of minutes. Compared with the steady arc ignitions during the ‘stable arcing period’ (Period 2 in Fig. 1), the random fluctuations (denoted as ③ in Fig. 1) presented in the ‘unstable arcing period’ will also probably be accompanied with the intermittent arc extinctions (①) and re-ignitions (②). In many cases, the stable and unstable arcing periods occur alternatively due to the unreliable contact between the conductors and the grounding surfaces.

The occurrences of HIAFs present continuous nonlinearity, giving rise to the waveform distortions and considerable harmonics [4]. As a result, detection algorithms based on these two features have been widely researched, including those utilizing the voltage-current nonlinear characteristics [5], as well as those based on the high-order harmonics [6], even harmonics [7], [8], odd harmonics [8], [9] and inter-harmonics [10]. Due to the temporal characteristics presented by waveform distortions of HIAFs, algorithms which unite the time and frequency domain, such as Hilbert-Huang transform [11], wavelet transform [12], [13] and some other time-frequency analysis methods [14], have been applied to the fault detections. To improve the reliability of the HIAF detections when fault features vary much under different situations, artificial intelligent algorithms, such as expert systems [15], [16] and neural network [4], [17] have also

Manuscript received January 21, 2019; revised April 30, 2019; accepted June 24, 2019. Date of publication August 14, 2019; date of current version March 24, 2020. This work was supported in part by the National Key R&D Program of China under Grant 2017YFB0902800 and in part by the Science and Technology Project of State Grid Corporation of China under Grant 52094017003D. Paper no. TPWRD-00097-2019. (Corresponding author: Hengxu Zhang.)

M. Wei, F. Shi, H. Zhang, and Z. Jin are with the Key Laboratory of Power System Intelligent Dispatch and Control of the Ministry of Education, Shandong University, Jinan 250061, China (e-mail: wmj_sdu@163.com; shifang@sdu.edu.cn; zhanghx@sdu.edu.cn; jzshuai@sina.com).

V. Terzija is with the School of Electrical and Electronic Engineering, The University of Manchester, Manchester M13 9PL, U.K. (e-mail: vladimir.terzija@manchester.ac.uk).

J. Zhou and H. Bao are with the State Grid Shanghai Municipal Electric Power Company, Shanghai 200233, China (e-mail: zhou.j@sh.sgcc.com.cn; baohl@sh.sgcc.com.cn).

Color versions of one or more of the figures in this paper are available online at <http://ieeexplore.ieee.org>.

Digital Object Identifier 10.1109/TPWRD.2019.2929329

been utilized. However, the data deficiency of field HIAFs has greatly hindered the practical application of these training-based intelligent technologies.

In the literature, most used arc models can only simulate the ‘stable arcing period’ [3], [4], [18] and the feature descriptions of the HIAFs were usually with ‘stable arc’ assumptions or neglected the ‘unstable’ situations [20], [21]. Therefore, the analysis results could not be completely applicable in the ‘unstable arcing period’ for its intense randomness and unpredictable intermittence, adding risks to the reliability of the model-based detection algorithms. Furthermore, difficulties still exist in providing reliable detection criteria when features of HIAFs vary under different situations, and meanwhile ensure the security that won’t send tripping signals when normal (non-fault) events happen. In addition, the present situation that waveform data is mainly achieved from the substations also restricts the detection reliability for the HIAFs happening far away.

However, with the increasing complexity, variability and uncertainty of the distribution network, it is a trend that the high-resolution measurement units [22] will be promoted at the distribution level [23], [24] to improve the system observability and further enhance the fault detection ability. In China, a distribution-level PMU (D-PMU) has been developed, tested and generally promoted since 2011 [25], and it is currently improved as a multi-functional measurement terminal to provide low-latency, high-resolution, time-calibrated and synchronous measurements (waveforms are included). Fault diagnosis, including the detection of HIAFs, is one of the advanced applications supported by the D-PMUs. Furthermore, with the development of the communication techniques, such as 5G wireless network, it is possible that the required signals, especially waveforms, can be uploaded more rapidly to further raise the fault diagnosis efficiency.

By analyzing the HIAFs in the field of 10 kV distribution system, this paper presents an improved arc model which can describe the randomness and intermittence characteristics of unstable arcing period. A unified harmonic energy is defined to distinguish HIAFs from the non-fault events, so that the detection security can be better guaranteed. Based on the unified harmonic energy, a global randomness index is proposed to quantitatively describe the harmonic variations during the unstable arcing period. A waveform distortion extraction method considering the distribution of detailed signals reconstructed by DWT is also presented. An integrated detection algorithm based on the above feature description methods is introduced. The application of the proposed integrated algorithm in the distribution network is introduced and demonstrated with D-PMUs. Reliability and security of the algorithm are discussed by comparing with some other algorithms using PSCAD simulations and field tests.

The rest of the paper is organized as follows. Section II introduces the implementation of the improved arc model, based on which the features of HIAFs are analyzed. In Section III, an integrated detection algorithm for HIAF containing two separated detection branches is proposed. In Section IV, the verification of reliability and security are carried out. Finally, conclusions are drawn in Section V.

II. FEATURE ANALYSIS OF HIAF

A. An Improved Arc Model

Imitation of the HIAF is commonly based on the arc models, which are mainly classified as:

- 1) The black-box models based on the thermal balance equations, like the classic Cassie [26], Mayr [27] arc models, and their improvements such as the Schavemaker [18] and Schwarz [19] arc models.
- 2) Models with the combination of power electronics components like diodes and DC voltage sources [3], [4].
- 3) Other models based on the experimental experiences [28], [29].

Most of the used arc models can simulate the stable arc ignitions but ignore the implementation of randomness and intermittence during the unstable arcing period, which are realized in this paper by adding the random coefficient RC to the Mayr arc model:

$$\frac{1}{g_{arc}} \left(\frac{dg_{arc}}{dt} \right) = \frac{1}{\tau_0} \left(\frac{u_f \cdot i_f}{P_{Loss0} RC} - 1 \right) \quad (1)$$

where, g_{arc} represents the equivalent conductance of arc ($1/\Omega$), u_f and i_f respectively represent the arc voltage (kV) and current (kA), τ_0 and P_{Loss0} respectively represent time constant (s) and stable dissipated power (MW). The random coefficient RC is described as:

$$\begin{cases} RC = RC_{ign}, & \text{if } RC_{sel} = 0 \\ RC = RC_{ext}, & \text{if } RC_{sel} = 1 \end{cases} \quad (2)$$

where RC_{sel} , RC_{ign} and RC_{ext} are three random variables. The selector RC_{sel} selects 0 and 1 with probability of q_0 and q_1 ($q_0 + q_1 = 1$) every pT seconds ($p \in [0.5, 1.0]$, representing the random occurrence time of arc extinction and re-ignition. $T = 0.02s$ when the fundamental frequency is 50 Hz). RC_{ign} and RC_{ext} respectively represent the dissipated power coefficient of ignition and extinction, indicating the variations of originally constant dissipated power P_{Loss} ($P_{Loss} = P_{Loss0} RC$), within which the arc will present the ignition or extinction state, respectively. The two coefficients can be expressed as:

$$\begin{cases} RC_{ign} \in \left(\frac{k_1 P_{Loss0}}{P_{Loss0}}, \frac{k_2 P_{Loss,bdy}}{P_{Loss0}} \right) \Rightarrow \left(k_1, \frac{k_2 P_{Loss,bdy}}{P_{Loss0}} \right) \\ RC_{ext} \in \left(\frac{k_3 P_{Loss,bdy}}{P_{Loss0}}, \frac{k_4 P_{Loss,bdy}}{P_{Loss0}} \right) \end{cases} \quad (3)$$

where $P_{Loss,bdy}$ represents the boundary dissipated power, whose value needs to be attempted with simulations. The simulated arc is in the ignition state when $P_{Loss} < P_{Loss,bdy}$ while in the extinction state when $P_{Loss} > P_{Loss,bdy}$. The random variations of amplitudes and distortion degrees can be realized by regulating the parameters of $k_1 \sim k_4$ according to simulation requirements (suggested ranges are set as $0.5 \leq k_1 \leq 1$, $0.8 \leq k_2 < 1 < k_3 < k_4$).

The improved Mayr arc model is established as Fig. 2, where R_T represents the transition resistance, and $t_{f,stable}$ represents the start time of stable arcing period. Suppose that the fault begins (t_f) with the unstable arc, and set $R_T = 0$,

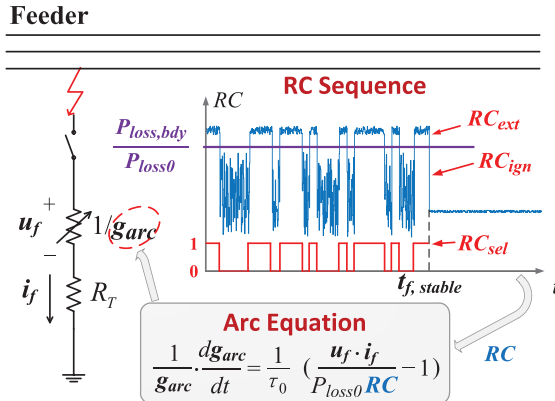


Fig. 2. Improved Mayr arc model.

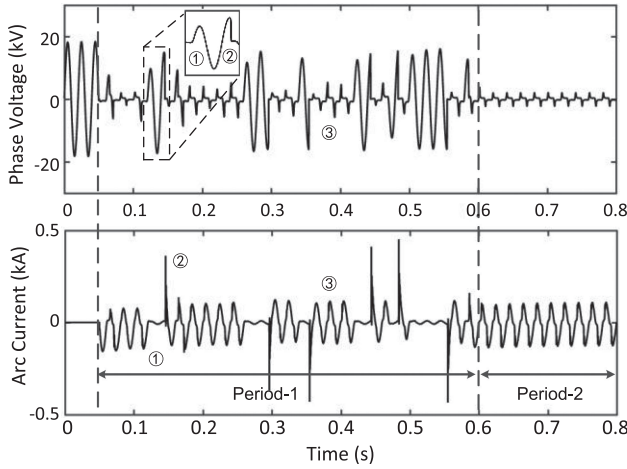


Fig. 3. Waveforms simulated by the improved Mayr arc model.

$t_f = 0.05$ s, $t_{f,stable} = 0.6$ s. Then waveforms of the faulty phase voltage and fault current are shown in Fig. 3. Compared with the waveform of field arc fault shown in Fig. 1, the intermittent arcing dynamic process and random fluctuation characteristics can be reflected to a certain extent.

Moreover, the proposed implementation of randomness and intermittence can not only be applied to the Mayr arc model, but also to other Mayr-type arc models based on the similar thermal balance equations. For example, the Cassie arc model can be improved as the following equation

$$\frac{1}{g_{arc}} \left(\frac{dg_{arc}}{dt} \right) = \frac{1}{\tau_0} \left(\frac{u_f^2}{u_{Loss0}^2 RC} - 1 \right) 1 \quad (4)$$

and its waveform comparison with a field arc fault is shown in Fig. 4, where the variations of waveform distortions can also be reflected.

B. Description of Fault Features

In many proposed algorithms [14], [30], [31], phase currents are used to extract the features of HIAFs, which, however, can be easily covered by the load components. Moreover, harmonics

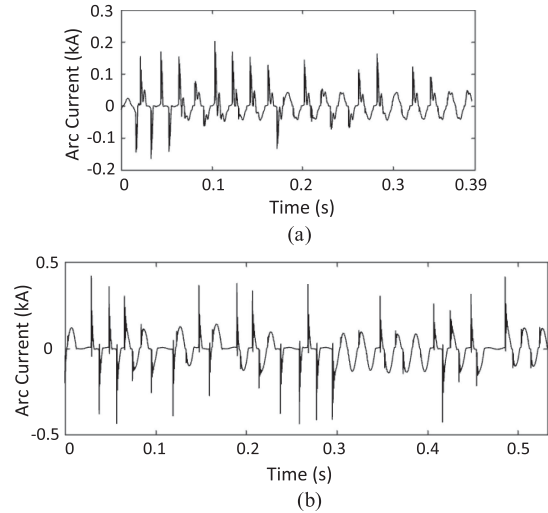


Fig. 4. Comparison between the simulated and field waveforms: arc current of (a) field arc, (b) simulated arc with improved Cassie model.

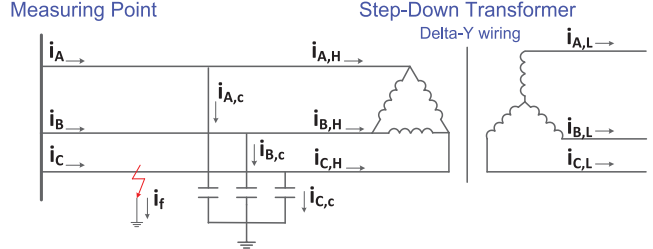


Fig. 5. Network with the D-Y wiring step-down transformer.

and randomness produced by the loads can also greatly affect the reliability and security of a HIAF detection algorithm if using the phase currents.

Zero sequence current is known as the superposition of three phase currents, and has been applied in many practical protections. In the medium-voltage distribution system, loads are commonly supplied through a step-down transformer, the high-voltage side of which is commonly known to be wired without neutral lines (Y or delta wiring [5]), especially at the 6–35 kV system in China. Therefore, the zero sequence current at the high-voltage side will not be affected by the low-voltage loads. It is illustrated by supposing the delta wiring at the high-voltage side (Fig. 5). With filtering of the delta wiring, sum of load currents $i_{X,H}$ ($X = A, B, C$) at the high-voltage side always equals to zero, and the zero sequence current i_0 at the ‘measuring point’ is calculated as:

$$3i_0 = i_A + i_B + i_C = i_{A,c} + i_{B,c} + i_{C,c} + i_f \quad (5)$$

where, i_X represents the phase currents at the measuring point, i_f represents the fault current, $i_{X,c}$ represent the leakage currents through the line to ground capacitors.

That is to say the zero sequence current mainly consists of the unbalanced component of the three phase capacitor leakage currents and the fault current, where the former mainly

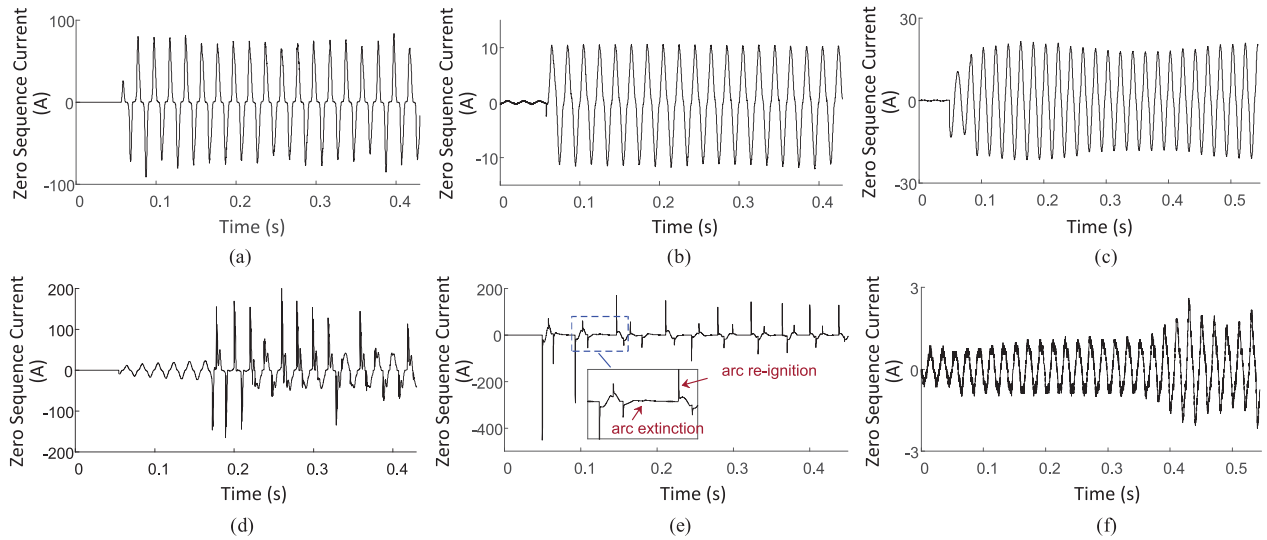


Fig. 6. The zero sequence currents of field HIAFs tested in a 10 kV system (HIAFs all happen at 0.05 s), (a) Type-1, grounded with wet soil, (b) Type-1, grounded with dry asphalt, (c) Type-1, grounded with wet cement, (d) Type-2A, grounded with pole, (e) Type-2B, grounded with dry soil, (f) Type-3, grounded with dry cement.

depends on the unbalanced network and is commonly small at the medium-voltage system.

Features of HIAFs vary greatly under different situations, including materials of grounding surfaces, system operations, surface humidity, and weather conditions. According to the analyses of the field tests in a 10 kV system (50 Hz system, introduced in Appendix A), HIAFs can be divided into the following types:

Type-1: After fault happens, the arc is with short ‘unstable arcing period’ and comes into the ‘stable arcing period’ very early. When grounded with different surfaces, both the fault distortions and current amplitudes could be various as shown in Fig. 6(a), (b) and (c). As the current decreases, the distortions are more likely to be smoother.

Type-2: The arc is with longer ‘unstable arcing period’ compared with the Type-1. Furthermore, the HIAFs only with random fluctuations are further classified as Type-2A (Fig. 6(d)), while those both with random fluctuations and intermittences are classified as Type-2B (Fig. 6(e)). Although Fig. 6(a) and (c) also present some fluctuations, they are still regarded as Type-1 for much lower randomness.

Type-3: For some HIAFs, due to the unbalanced operations or the extremely high grounding impedance, amplitudes of post-fault zero sequence current may have few differences between that of the pre-fault (Fig. 6(f)). In this case, the current amplitude is much lower and waveform distortions may be covered by the non-fault components more or less, leading to more difficulties in the detections.

Diverse types of HIAFs and their performances make it challengeable for an algorithm to always keep high detection reliability with just single feature description and identification method.

As introduced in Section I, harmonics, randomness and waveform distortions are three most predominant features of HIAFs. Firstly, harmonics present abnormalities both during the

stable and unstable arcing period. However, as shown in Fig. 6, significantly different amplitudes or percentages of harmonics can be presented because the magnitudes and distortion degrees of currents vary under different conditions. A better definition of harmonic intensity is important to guarantee the detection reliability and security at the same time.

Secondly, also demonstrated in Fig. 6, the occurrence, duration and fluctuation range of unstable arcs are all uncertain for HIAFs. Moreover, fault arcs sometimes can be self-extinguished or extinguished by the arc-suppression devices in seconds. As a result, only utilizing randomness features cannot detect the HIAFs beginning with stable arcs or detect them as soon as possible.

Finally, waveform distortions also exist in almost all types of HIAFs with different shapes and degrees. However, as shown in Fig. 6(d) and (e), the distortions of these Type-2 HIAFs are much more irregular, making it more difficult for the distortion characteristics to be correctly described.

As a result, it is necessary to combine the multiple features to respectively detect HIAFs beginning with unstable or stable arcs, and keep reliability under different fault conditions. Meanwhile, it is equally important to guarantee the detection security at the same time to avoid the unnecessary blackouts.

III. INTEGRATED DETECTION ALGORITHM

In this section, two description methods for the features of HIAFs are presented, including a global randomness index to reflect variations of the defined unified harmonic energies, and a DWT-based method to extract distortions.

A. Global Randomness of Unified Harmonic Energy

Harmonic is a useful characteristic quantity to describe the randomness generated by HIAFs. In some traditional algorithms,

randomness characteristic is extracted by finding the point-to-point changes between the present harmonic amplitudes and historical values [30]–[32]. However, as mentioned in last section, problems exist because HIAFs contacting various surfaces can produce significantly different amplitudes of currents. As a result, if using amplitudes directly, distinctions can hardly be found out between non-fault disturbances and the HIAFs with very limited current.

It was proved that low order harmonics can make remarkable performances in reflecting arc features [7]–[10]. In this paper, 2nd–5th orders of harmonics are used to define a unified harmonic energy:

$$\begin{cases} E_1^u = 1 \\ E_k^u = E_k / E'_1, k \neq 1 \\ E_k = \sum_{i=2}^5 \left(\frac{X_k^F(i) / X_k^F(1)}{X_N^N(i) / X_N^N(1)} \right) \\ E'_1 = \min\{E_1, \text{cof}_{\lim} \sum_{i=2}^{k_{\text{window}}} E_i / (k_{\text{window}} - 1)\} \end{cases} \quad (6)$$

where, E_k represents the harmonic energy of the k^{th} cycle, and E_k^u represents the unified harmonic energy. $X_k(i)$ represents amplitude of the i^{th} harmonic order. Superscript F marks the variables after fault while N marks those at non-fault situations. k_{window} represents the length of detection window commonly set as 10 ~ 15 cycles. cof_{\lim} represents the limitation of E_1 in case of its extremely large values.

Fig. 7(a)–(c) presents the comparisons of three different harmonic definitions from amplitudes to unified harmonic energies by illustrating with the HIAFs in Fig. 6, and two non-fault events that can affect the zero sequence currents. One non-fault event is the capacitor switching, affecting the zero sequence current due to its asynchronous operations. The other event is the motor start of wind turbine which connects with the network through Yn-Yn wiring transformer for control requirements [33], [34], so that the fluctuations caused by wind turbines can be transmitted across the transformer and affect the zero sequence current at high-voltage side.

According to equation (6), harmonic energy E_k is defined by comparing harmonic amplitudes with the fundamental components, so that harmonic energies with different scales of current amplitudes will not vary significantly (compare Fig. 7(b) with (a)). Furthermore, due to much higher harmonic attenuations of non-fault events shown in Fig. 7(b), the harmonic energies E_k would drop dramatically and persist at a lower level (Fig. 7(c)) after being unified as E_k^u by taking E_1 as the base.

Based on the defined unified harmonic energy, a global randomness index $RAND$ is expressed as:

$$RAND = \sum_{k=3}^{k_{\text{window}}} |E_k^u - E_{k-1}^u| / (k_{\text{window}} - 2) \quad (7)$$

which reflects the general variation of unified harmonic energy within the detection window.

To avoid the harmonic changes caused by great attenuations in non-fault events, the summation in equation (7) starts from $k = 3$ or a bit later. Afterwards, randomness indexes of the events in Fig. 7(c) are further calculated and presented in Fig. 7(d). If the

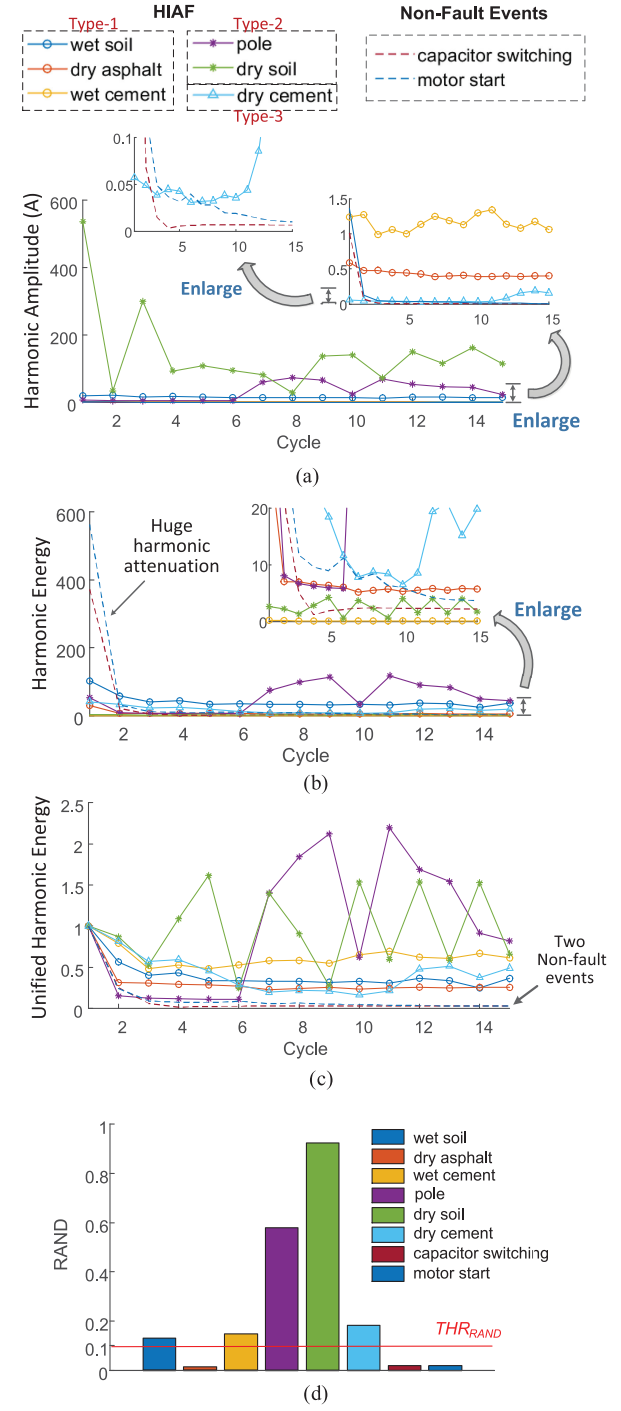


Fig. 7. Comparisons of three harmonic definitions for HIAFs and non-fault events: (a) defined directly with harmonic amplitudes, (b) defined with harmonic energies, (c) defined with unified harmonic energies, (d) global randomness index. All calculated with the sum of 2nd–5th harmonics.

threshold (denoted as THR_{RAND}) is set as 0.1, the exhibited HIAFs can all be distinguished from non-fault events except for the extremely stable one contacting with the dry asphalt, whose waveform is shown in Fig. 6(b).

It is emphasized that purpose of the global randomness index is to detect all the Type-2 HIAFs and detect those of Type 1 as

many as possible on the premise of detection security. According to the statistical analysis (Fig. 18 in Appendix B), $RANDs$ of the non-fault events are mostly under 0.1 while those of HIAFs are mostly above 0.1. To fully guarantee the detection security, the THR_{RAND} can be set around 0.2. The HIAFs that cannot be detected by the global randomness index are demonstrated to have relatively stable distortions, which can be suitable for the detection method proposed in the following Section III-B.

B. Waveform Distortion Extraction

The global randomness index based on unified harmonic energy can perform well in identifying the *Type-2* HIAFs that begin with unstable arcing period, but obviously cannot reliably settle the HIAFs coming into the stable arcing period early (*Type-1* and some *Type-3*). In this section, the discrete wavelet transform (DWT) is used to figure out this problem by detecting HIAFs with waveform distortions.

DWT is a tool which resolves signals into time and frequency, making it convenient to analyze the local features with different frequency components. For a sampling signal $s[n]$, its DWT is expressed as:

$$W_{a,b}[n] = \sum_n s[n] \cdot \frac{1}{\sqrt{a}} \psi \left[\frac{n-b}{a} \right] \quad (8)$$

where, $\psi[n]$ is the wavelet base. The coefficient a and b are the scale and displacement factors. A wavelet transformed signal in the selected frequency band $[f_1, f_2]$ can be defined as:

$$WT_{fb}[n] = \left| \sum_a \sum_b W_{a,b}[n] \right|, a \in \left[\frac{f_1}{f_S}, \frac{f_2}{f_S} \right] \quad (9)$$

where f_S is the sampling frequency.

In this section, with db4 wavelet adopted as the wavelet base, Fig. 8(a) shows the zero sequence current of a simulated Type-3 HIAF ($R_T = 2 k\Omega$). The waveform distortion interval is generally named zero-off or zero-crossing period (ZCP, normally two ZCPs per cycle). As Fig. 8(b) shown, its wavelet transformed signal reconstructed by band of $2 k\sim 3 kHz$ presents the spike features during the ZCPs, which is extracted and quantitatively described as follows:

$$\begin{aligned} R_{ZCP}^k &= \sum_{ZCP1+ZCP2} WT_{fb}^k[n] / \sum_{n_0}^{n_0+N_T} WT_{fb}^k[n] \\ &= \sum_{ZCP} WT_{fb}^k[n] / \sum_T WT_{fb}^k[n] \end{aligned} \quad (10)$$

where k represents the number of post-fault cycle, N_T and n_0 respectively represent the total number of sampling points in a cycle and the first point of each cycle. If the two requirements in equation (11) are met for several successive cycles (denoted as THR_{count} , commonly set as 4), the fault is believed to happen.

$$\begin{cases} R_{ZCP}^k \geq THR_R \\ \sum_{ZCP} WT_{fb}^k[n] \geq THR_{amp} \\ THR_{amp} = \sum_{k=1}^{k_{window}} \sum_{ZCP} WT_{fb}^k[n] / k_{window} \cdot coef_{amp} \end{cases} \quad (11)$$

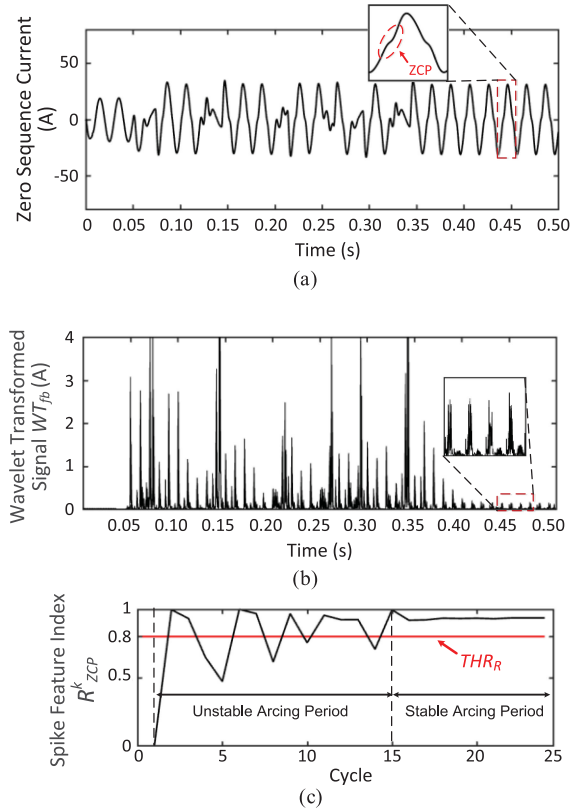


Fig. 8. Spikes during the waveform distortions in the transformed signal: (a) Zero sequence current of a HIAF, (b) Signal after wavelet transform, (c) R_{ZCP}^k (stable arcing period starts after the 15th cycle, at 0.35 s).

where THR_R reflects the dominated ratio of amplitudes during ZCPs in a cycle, and THR_{amp} is to eliminate the cycles whose amplitudes during the ZCP is far below the average. For a stable HIAF, its spikes of reconstructed signal are concentrated around the ZCPs, its R_{ZCP}^k during the stable cycles can thereby persist at higher values. According to Fig. 8(c) and the statistical analysis shown in the Fig. 19 of Appendix B, R_{ZCP}^k of HIAFs are theoretically close to 1 and a bit lower due to the noise or some other interferences, while that of the non-fault events are slightly higher than 0.5. As a result, THR_R can be set around 0.80.

However, the effective description of this distortion index needs: 1) correct localization of the distortion intervals, 2) good immunity against noise.

In numerical simulations, the relative positions of distortion intervals in a cycle are fixed if using a certain arc model. Apparently, it is unrealistic for a real fault due to its varieties (like two HIAFs in Fig. 9(a) and (b)). Therefore, a Distortion-Tracking method is proposed to locate the unpredictable distortion intervals cycle by cycle. The method is illustrated with the zero sequence current and the ZCPs. As shown in Fig. 9, the relative position of each ZCP usually varies around the corresponding zero-crossing point. As a result, the tracking range for each ZCP is with the length of $3T/4$, and makes zero-crossing point as its midpoint. In the tracking range, search for the interval with length of $T/4$ (the distortion of a HIAF commonly lasts for $T/10 \sim T/4$ [5]) which possesses the sharpest spikes (e.g., the maximal

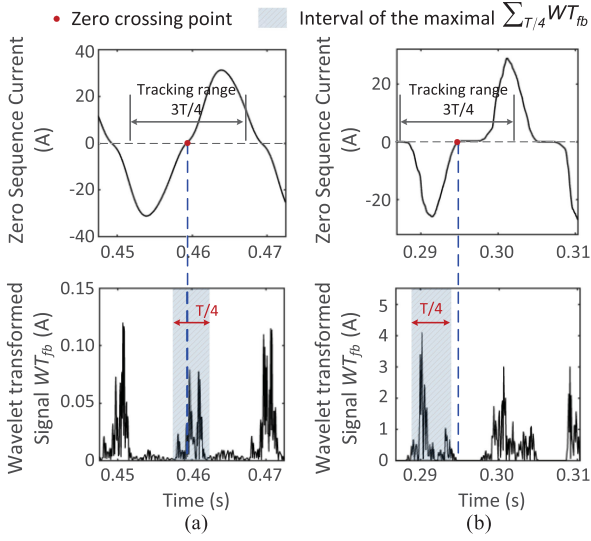


Fig. 9. Distortion-Tracking: (a) and (b) are two field HIAFs.

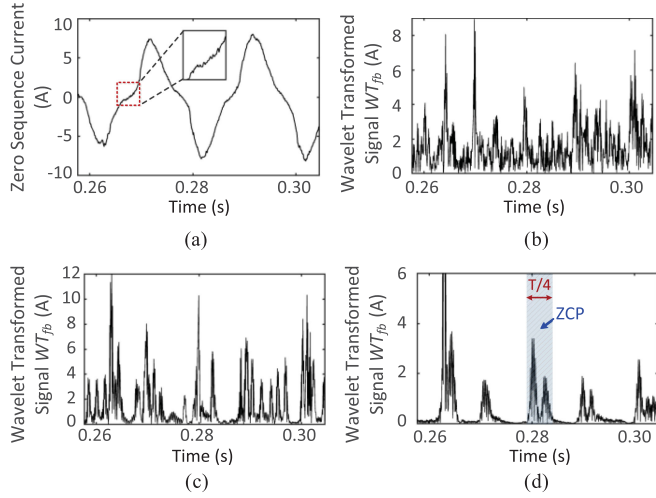


Fig. 10. Signal filtering: (a) raw signal of a field HIAF, (b), (c) and (d) are $WT_{fb}[n]$ of filtered signal respectively with traditional digital filter (illustrated by median filter), wavelet filter (fixed threshold estimation) and wavelet filter (minimax threshold estimation).

$\sum_{T/4} WT_{fb}^k[n]$), and this interval will be marked as the ZCP of this zero-crossing point.

Noise immunity is significant for an algorithm applied in the distribution system. Compared with the global randomness index that is based on the low-order harmonics, the DWT-based extraction method for waveform distortion is usually more sensitive to the noise even after filtering.

Firstly, the raw signal needs to be filtered. Compared with traditional digital filters, those utilizing the wavelets perform much well in separating the effective components and noise in the selected frequency bands (compare Fig. 10(b) with (c) and (d)). Moreover, by limiting the wavelet coefficients with soft and minimax thresholds [36], spikes during the distorting intervals can be much clearer (compare Fig. 10(d) with (c)) and easier to be extracted.

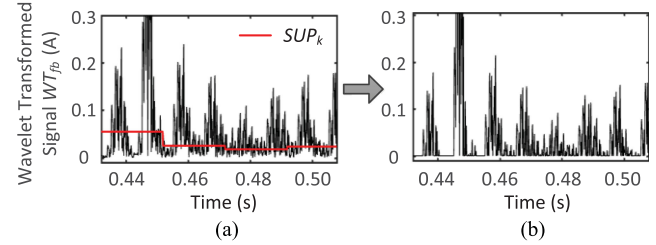


Fig. 11. Noise suppression applied to wavelet transformed signal: (a) The transformed signal of a HIAF with 25 dB noise after filtering, (b) The transformed signal after noise suppression.

Secondly, an adaptive noise-suppression is applied according to total amplitudes of $WT_{fb}^k[n]$ in each cycle and the calculated noise intensity (equation (12)) so as to further weaken the noise influences (see Fig. 11).

$$\begin{cases} WT_{fb}^k[n] = \max\{WT_{fb}^k[n] - SUP_k, 0\} \\ SUP_k = \sum_T WT_{fb}^k[n]/coef_{sup} \\ coef_{sup} = f(SNR) \end{cases} \quad (12)$$

where $coef_{sup}$ represents the noise suppression coefficient and depends on the computed noise intensity described by signal-noise ratio (SNR). The statistical analysis shown in Fig. 20 of Appendix B is adopted with different $coef_{sup}$ and SNR. In the figure, the function $f(SNR)$ in equation (12) is suggested to keep the successfully detected rate of the total 369 simulated HIAFs over 95%. The spike features produced by HIAF distortions and noise components can be correctly separated when SNR is over 15 dB. However, when SNR is below 15 dB, detection rate will rapidly decrease, and if further lowering the $coef_{sup}$ below 1, the detection security cannot be guaranteed any more.

According to Fig. 8(c), compared with the global randomness index, the proposed distortion extraction method cannot always ensure the detection reliability for HIAFs in the unstable arcing period (before 15th cycle) due to its more complicated distortions. As a result, it is necessary to exploit the superiorities of the two branches in Section III-A and B respectively for the unstable and stable arcs, in order to complement with each other and improve the detection reliability for different types of HIAFs.

C. The Integrated Detection Flow

Based on the feature description methods, flow of the integrated detection algorithm for HIAFs is shown in Fig. 12, and the specific steps are instructed as follows:

Step 1. Start: If a disturbance is detected, waveforms of zero sequence current will be recorded, and filtered by wavelet filters with minimax thresholds mentioned in Section III-B.

Step 2. Unified Harmonic Energy: Apply fast Fourier transform (FFT) to get harmonic amplitudes of 2nd ~ 5th orders and calculate the unified harmonic energy E_k^u of each cycle within the whole detection window according to equation (6).

Step 3. Randomness Analysis (RA): Calculate the global randomness index as equation (7). Output the result,

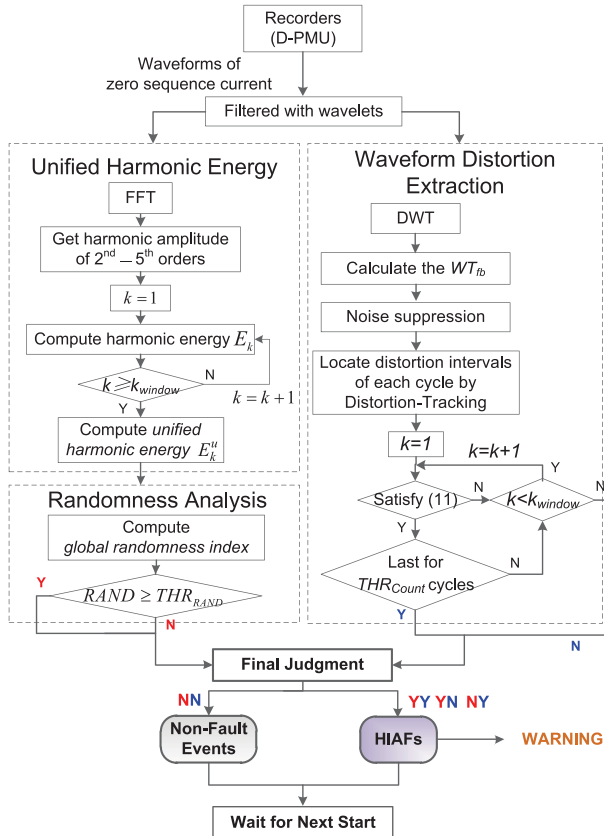


Fig. 12. Flow of the integrated detection algorithm for HIAF.

which is ‘Y’ if the index reaches over the threshold, and otherwise, is ‘N’.

Step 4. Waveform Distortion Extraction (WDE): This step proceeds simultaneously with Step 2 after waveforms uploaded. Then, obtain the wavelet transformed signals, apply the noise suppression and locate the distortion intervals. Describe the spike features as equation (10), and if the requirements in equation (11) are satisfied for THR_{count} cycles successively, a result of ‘Y’ is output.

Step 5. Final Judgment: According to the result from two detection branches, the principle of final judgment is also shown in Fig. 12. HIAFs will be confirmed if the final results are ‘YY’, ‘YN’ or ‘NY’.

IV. CASE STUDY

A. D-PMU-Based HIAF Detection System

In the practical application, the proposed HIAF detection algorithm is integrated as a modular named ‘HIAF Detection’ in a D-PMU based monitoring and management system (shown in Fig. 13). The system is established to set up a systematic operation procedure and support the HIAF detection and other required applications in the continuous complex and diversified distribution network.

The D-PMU based system includes the Local Measuring Terminal and the MAIN STATION of PMU Data. The Local Measuring Terminal is mainly comprised of distribution-level PMUs (D-PMUs), which can calculate and transmit real-time phasors to the MAIN STATION every 20 ms (for 50 Hz system). Meanwhile, at most 30 minutes of waveforms are recorded by D-PMUs with sampling frequency of 6.4 kHz. The waveforms will be uploaded according to the orders from the MAIN STATION. With these data, Fault Diagnosis including the HIAF detection and other fault detection/location functions can be realized. More managements and controls of the distribution system can also be established with data support of D-PMUs [37], such as the State Estimation, Security Assessment and Coordinated Control.

The D-PMU based system can be applied on the basis of traditional SCADA based Distribution Automation System (DAS) with necessary data exchanges (like step ①.A and ⑧ marked in Fig. 13). The relative independent relationship between DAS and the novel D-PMU based system makes the revolution be more easily promoted without greatly changing the traditional DAS operation structures.

By combining the proposed algorithm with the system, the HIAF detection can be implemented as following steps: With the real-time data transmit from different D-PMUs, MAIN STATION firstly carries out the Initial Detection (step ②). This step is to screen out the faults with high-level currents, which can be detected and located with no need of waveforms. For the weak and indeterminable disturbances probably caused by faults like HIAFs, a start signal will be sent (step ③) and waveforms will be called up from the specific D-PMUs (step ④ and ⑤), containing 15 cycles before the disturbance happening and 25 cycles after that. If a HIAF is detected in the modular of HIAF Detection by using the proposed algorithm (step ⑥), the further location for HIAF will pursue (step ⑦), the method of which is one of our future researches. Finally, with result (step ⑧) about the exact position of a HIAF achieved, tripping operation will be carried out by the DAS in the step ⑨.

For the D-PMU based system, disturbances are firstly analyzed by the modular of Initial Detection in the MAIN STATION, many large disturbances caused by faults or non-fault events can be directly detected and located, so that waveforms needn’t be frequently uploaded any more. Moreover, the uploaded waveforms by D-PMUs are synchronous and time-calibrated, which also present great superiorities compared with the traditional digital recorders for their various degrees of time-delays.

B. Reliability Verification

Reliability of a fault detection algorithm represents the ability that a fault can be identified as long as it occurs. As a result, the proposed detection algorithm is required to be able to detect HIAFs of different types under different situations, including neutral grounding modes, grounding surfaces, transition resistances and fault locations.

Verification of reliability is carried out with both simulated and field HIAFs due to the restricted number of real data.

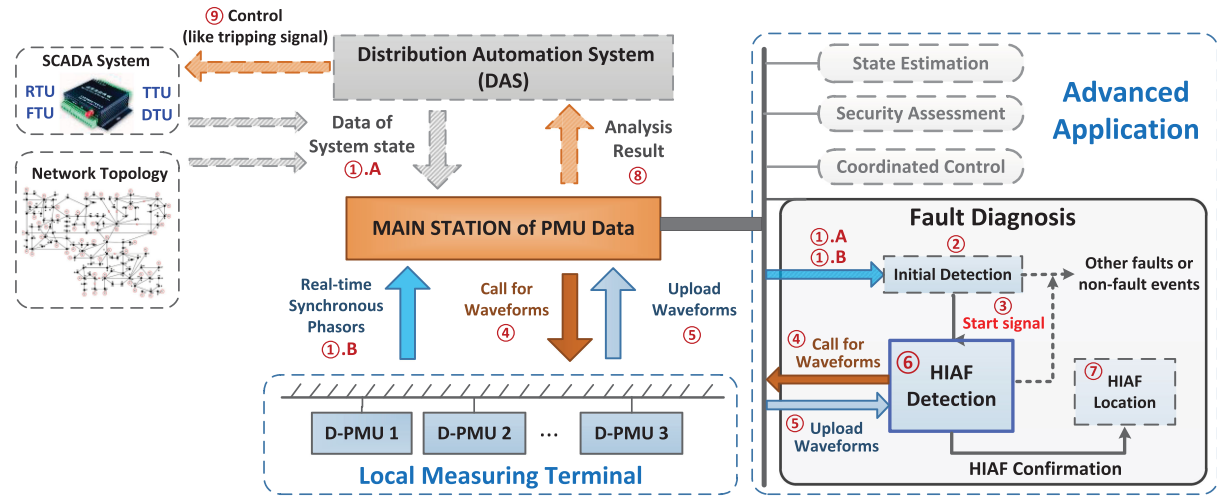


Fig. 13. Data flow of the D-PMU based system for HIAF detection.

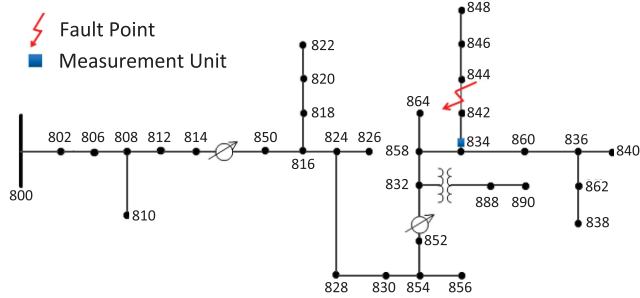


Fig. 14. Diagram of the IEEE-34-bus network.

Firstly, an example of the simulated Type-3 HIAF is illustrated to introduce the algorithm implementation and effectiveness in detail. With IEEE34-bus network (Fig. 14) established in PSCAD, basic simulating parameters are set as:

Fundamental frequency is 50 Hz, noise added to zero sequence current is with SNR of 25 dB and the sampling frequency is 6.4 kHz.

The neutral grounding mode is set as isolated neutral, the fault is set at the mid of the line between bus-844 and bus-842 and the measurement point is installed at bus-834.

A Type-3 HIAF with $R_T = 2 \text{ k}\Omega$ is added, the faulty phase is assumed as A, the fault time is set as 0.05 s and the stable arcing period occurs at 0.35 s.

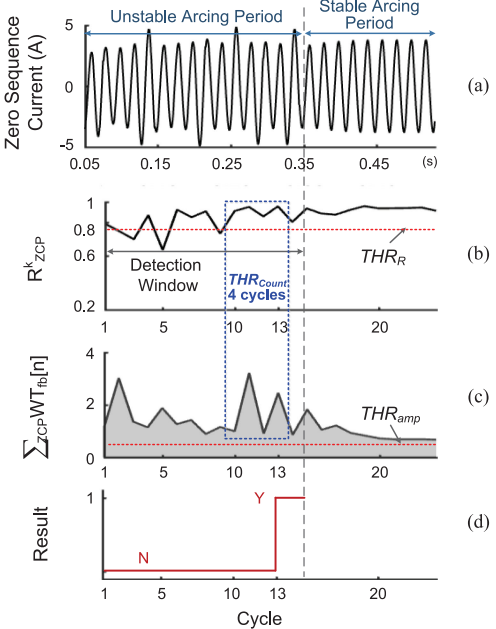
Parameters of the improved Mayr arc model are set as: $\tau_0 = 8 \times 10^{-4} \text{ s}$, $P_{Loss0} = 1 \times 10^4 \text{ W}$, $P_{Loss,bdy} = 4 \times 10^4 \text{ W}$, $k_1 = 1$, $k_2 = 0.8$, $k_3 = 1.075$, $k_4 = 1.1$, $p = 1$ and $q_0 = 0.3$.

Parameters of the algorithm are set as: $k_{window} = 15$, $THR_{RAND} = 0.20$, $THR_R = 0.80$, $coef_{amp} = 8$, $THR_{count} = 4$.

The unified harmonic energy of zero sequence current in each cycle during the detection window, as well as the global randomness index, are shown in Table I. Meanwhile, the results of waveform distortion extraction are shown in Fig. 15.

TABLE I
RESULT OF BRANCH RA

Cycle	1	2	3	4	5	6	7	8	9
E_k^u	1.000	1.906	0.478	1.370	1.304	0.337	0.392	1.277	1.665
Cycle	10	11	12	13	14	15	<i>RAND</i>		
E_k^u	0.430	1.295	1.349	1.696	1.363	1.595	0.5961 (Y)		

Fig. 15. Result of branch WDE, (a) waveforms; (b), (c) are the two criteria expressed in equation (11); (d) is the result of WDE. If criteria are satisfied for successively 4 (THR_{Count}) cycles, a 'Y' will be output.

With $RAND$ exceeding the THR_{RAND} , output of branch RA is 'Y'. According to Fig. 15(d), the output of WDE also is 'Y' because the two criteria in equation (11) are both satisfied.

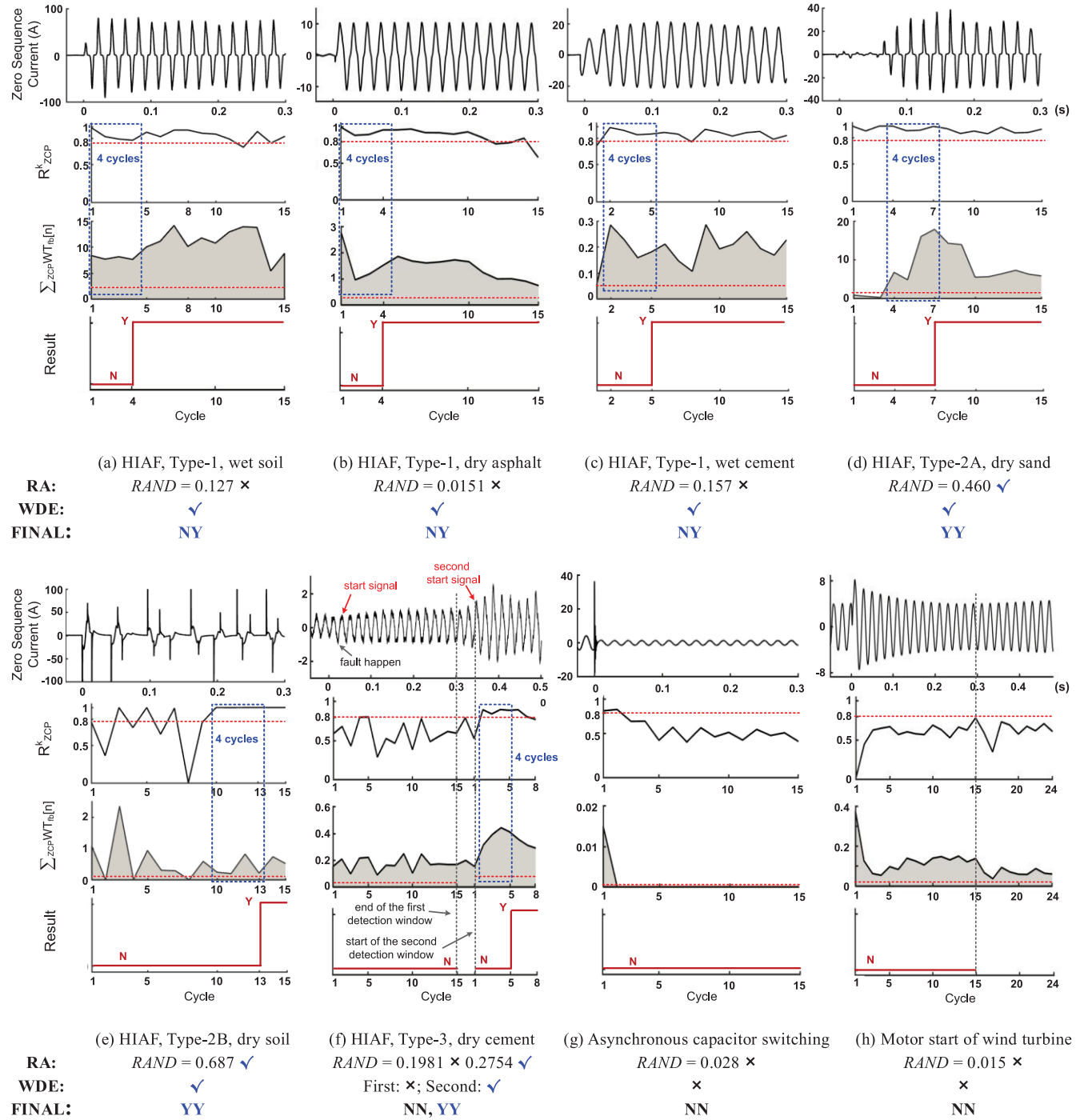


Fig. 16. Detailed detection results of HIAFs and non-fault events: results of branch WDE are shown by figures and conclude by texts under each figure, while results of branch RA are presented only by texts. The FINAL detection results are also presented with texts.

Therefore the final result of 'YY' can make the HIAF be successfully detected according to Step 5.

Secondly, the field HIAFs achieved by D-PMUs deployed in a 10 kV tested system mentioned in the Section II-B are also used to verify the reliability of the proposed algorithm. Totally 35 field HIAFs are achieved with three system neutral grounding modes and several fault grounding surfaces (introduced in

Appendix A). These different types of field HIAFs are classified according to Section II-B, and some of their detailed detection results are presented in Fig. 16(a)–(f). Statistical results of all the field and simulated HIAFs are shown in Section IV-D by comparing with other algorithms. With the combination of RA and WDE in the algorithm, most of the HIAFs can be reliably detected.

C. Security Verification

Security of a fault detection algorithm represents the ability that the disturbances caused by non-fault events can be distinguished from the faults. Otherwise, unnecessary system de-energizing will happen.

As explained in Section II-B, at the medium-voltage distribution system, effects on the measured zero sequence current caused by loads can be neglected after filtered by step-down transformers which are commonly without neutral lines at the high-voltage side. Therefore, the proposed algorithm will not be affected by the load-side disturbances, such as arc furnaces, whose step-down transformers have to be set as Y-delta or delta-delta wirings [38], [39]. However, as mentioned in Section III-A, some non-fault disturbances can still be reflected on zero sequence current, including 1) capacitor switching, whose asynchronous connections can result in the transient fluctuations of zero sequence current, and 2) operations of some wind turbines, whose inter-connecting transformers are sometimes wended as Yn-Yn wirings for the requirements of control strategies [33], [34]. The event 1) is with short transient process while that of the event 2) is longer.

A set of zero sequence current waveforms of the above two non-fault events are presented in Fig. 16(g)-(h), as well as their detection results by the proposed algorithms, which cannot be erroneously detected. As verified in Fig. 7 of Section III-A, the proposed randomness indexes of these events can be greatly weakened if based on the defined unified harmonic energies due to their rapid harmonic attenuations. On the other hand, the second branch of WDE will also not result in the mistakes because these non-fault events cannot generate continuous distortions.

Furthermore, statistical results of these non-fault events are presented in Section IV-D, also by comparing with other algorithms.

D. Comparison With Other Algorithms

As pointed out in Section II-B, diversities of the fault features make it difficult to keep the high reliability for different types of HIAFs and ensure the security at the same time. In the last several decades, a large number of researches and continuous improvements have been made to figure out better balances between the two requirements.

In this section, comparisons are carried out with the algorithms in [5], [13], [40] and [41], which typically represent the HIAF detection algorithms making use of the harmonic abnormalities, randomness, and distortions. Except for [5], phase currents are all used in these referred algorithms, the effectiveness of whom will therefore be greatly affected due to the coverage of load currents. However, in this section, the comparisons are all made by replacing phase currents with zero sequence current. That is to say the comparisons only consider their algorithm principles but not the used signals. Reliabilities are tested with 35 field HIAFs detected by D-PMUs in the 10 kV tested system and 63 numerically simulated HIAFs in PSCAD of the 369 samples introduced in Appendix B (Table II and Table III), while securities are tested with 54 non-fault events of the 90 samples introduced in Appendix B (Table IV).

TABLE II
RELIABILITY COMPARISON WITH FIELD HIAFS

Total	Successfully detected HIAFs				
	[13]	[40]	[41]	[5]	Ours
Type-1	12	9	11	6	12
Type-2A	6	6	4	3	3
Type-2B	7	7	0	1	0
Type-3	10	5	2	3	5
Total	35	27	17	13	20
	(77.1%)	(48.6%)	(37.1%)	(57.1%)	(91.4%)

TABLE III
RELIABILITY COMPARISON WITH SIMULATED HIAFS

Total	Successfully detected HIAFs				
	[13]	[40]	[41]	[5]	Ours
Type-1	15	13	12	13	15
Type-2A	9	9	2	5	3
Type-2B	9	9	7	2	9
Type-3	30	26	8	15	9
Total	63	57	29	35	36
	(90.5%)	(46.0%)	(55.6%)	(57.1%)	(96.8%)

TABLE IV
SECURITY COMPARISON WITH NON-FAULT EVENTS

Total	Successfully distinguished non-fault events				
	[13]	[40]	[41]	[5]	Ours
Event 1)	27	27	27	21	27
Event 2)	27	19	20	23	27
Total	54	46	47	44	54
	(85.2%)	(87.0%)	(81.5%)	(100.0%)	(100.0%)

Reference [13] is one of the algorithms which utilize the energies established by DWT coefficients, to extract the variations in the reconstructed signals by these coefficients. This algorithm can have good reliability when detecting the HIAFs of Type-1 and Type-2. However, it just focused on the ‘energy intensity’ of the reconstructed signals, but neglected their distributions, therefore the HIAFs with similar amplitudes comparing with non-fault conditions (Type-3) are not easy to be picked out, especially under the noisy environment. The algorithm in [40] detects HIAFs by utilizing the randomness of waveform distortions, can perform well in detecting HIAFs of Type-2A and a part of Type-1 and Type-3, but will be invalid for those with intermittence (Type-2B) or those with smoother distortions when contacting the lower-current surfaces. Reference [41] detects HIAFs by quantifying the similarity between the measured current and a preset current with typical HIAF distortions. However, the algorithm is too sensitive to the phase angles of currents and distortion shapes, so the reliability and security cannot be guaranteed at a higher level. Reference [5] proposed an algorithm extracting the distortions by voltage-current characteristic profiles, and has higher sensitivity for the Type-1 and most Type-3 HIAFs. However, when the distortions are irregular in Type-2 or occur in an unbalanced system (Type-3), the reliability cannot be guaranteed.

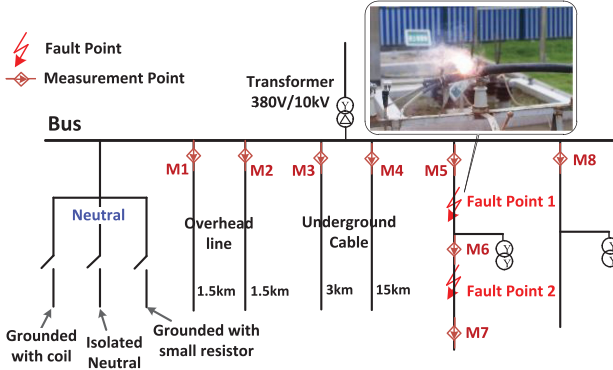


Fig. 17. Network topology of the 10-kV test system.

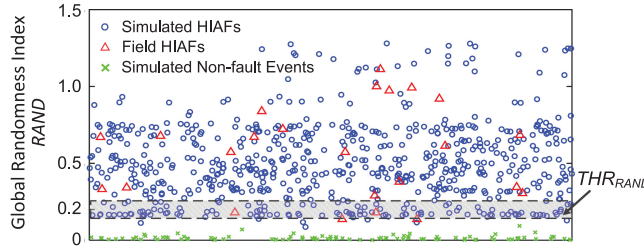


Fig. 18. Statistical result of the global randomness indexes for non-fault events, Type-2 and a part of Type-3 HIAFs: The simulated HIAFs are all simulated by the improved arc model, which are all with the unstable arcing periods.

As presented by the results from Table II to IV, the proposed integrated algorithm can reach a higher reliability for various types of HIAFs, as well as higher security.

V. CONCLUSION

In this paper, an improved arc model is proposed, which can realize the description of randomness and intermittence during the unstable arcing period of HIAFs. The suggested parameters of the arc model are presented. With the classification and feature analyses for different HIAFs, an integrated detection algorithm is proposed. In the algorithm, the defined unified harmonic energy can unify the quantitative descriptions for HIAFs under different situations, and enlarge the difference between faults and non-fault events. Subsequently, the global randomness index based on the unified harmonic energy and the feature extraction method based on DWT can respectively perform well in detecting different types of HIAFs, while their combination can ensure the greater reliability and security at the same time as the verification by comparing with other algorithms shows. The practical application of the proposed algorithm in a D-PMU based system is also introduced.

APPENDIX A

The field test system is a 10 kV network with a 380 V/10 kV transformer, whose topology is shown in Fig. 17. The load currents range from 15 A~30 A (RMS). D-PMUs introduced in the Section IV-A are deployed at the measurement points

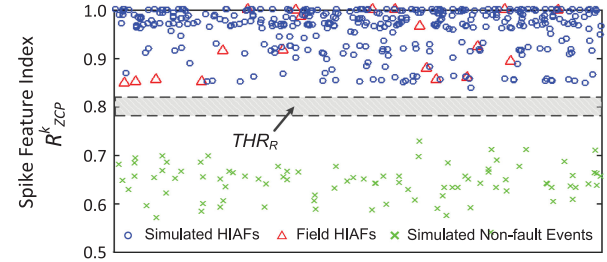
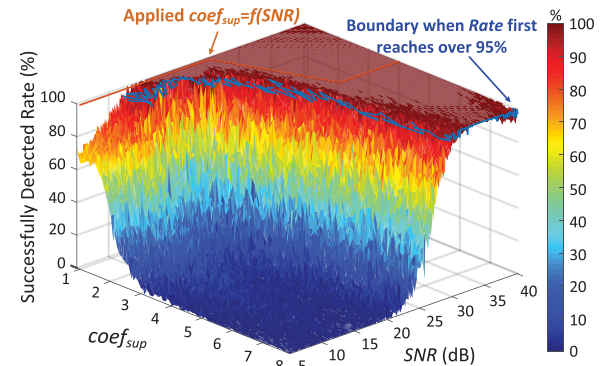
Fig. 19. Statistical result of R_{ZCP}^k (another 369 simulated Type-1 HIAFs with R_T from 1 Ω to 3 k Ω , which are all assumed with stable arcing periods).

Fig. 20. Statistical result of the detecting rate for stable arcs after applying noise suppression (the same group of 369 simulated HIAFs with Fig. 19).

marked in the typology, whose waveform sampling frequency is 6.4 kHz.

The HIAFs are tested in the ‘Fault point 1’ and ‘Fault point 2’ while the fault waveforms are achieved with the D-PMU installed at the position of M5. Distances between the two fault points and M5 are respectively 30 m and 100 m. Totally 35 HIAFs are tested by changing three different neutral grounding modes and grounding materials (dry/wet soil, dry/wet cement, dry/wet asphalt, dry/wet sand, pole and grass).

APPENDIX B

Appendix B presents several statistical results as the proofs of some arbitrary threshold settings. The statistical analyses are all carried out with simulated HIAFs, field HIAFs and simulated non-fault events including the capacitor switching and motor start of wind turbines.

The simulated HIAFs are achieved by simulating in the IEEE-34bus system (Fig. 14) with PSCAD with three different neutral grounding modes (isolated neutral, neutral grounded with suppression coil, and neutral grounded with small resistor), different fault transition resistances ranging from 1 k Ω to 3 k Ω , and different fault positions (at mid of line-844-842, line-812-814 and line-862-838, where the measurement points are set at bus834, bus808 and bus860 respectively). The field HIAFs are achieved in the test system introduced in the Appendix A. The totally 90 simulated non-fault events are also achieved in the IEEE-34bus system with different parameters of capacitor and motors.

REFERENCES

- [1] W. Zhang, Y. Jing, and X. Xiao, "Model-based general arcing fault detection in medium-voltage distribution lines," *IEEE Trans. Power Del.*, vol. 31, no. 5, pp. 2231–2241, Oct. 2016.
- [2] A. Ghaderi, H. L. Ginn, III, and H. A. Mohammadpour, "High impedance fault detection: A review," *Electr. Power Syst. Res.*, vol. 143, pp. 376–388, 2017.
- [3] S. Gautam and S. M. Brahma, "Detection of high impedance fault in power distribution systems using mathematical morphology," *IEEE Trans. Power Syst.*, vol. 28, no. 2, pp. 1226–1234, May 2013.
- [4] A. Soheili and J. Sadegh, "Evidential reasoning based approach to high impedance fault detection in power distribution systems," *IET Gener. Transmiss. Distrib.*, vol. 11, no. 5, pp. 1325–1336, Mar. 2017.
- [5] B. Wang, J. Geng, and X. Dong, "High-impedance fault detection based on nonlinear voltage-current characteristic profile identification," *IEEE Trans. Smart Grid*, vol. 9, no. 4, pp. 3783–3791, Jul. 2018.
- [6] D. P. S. Gomes, C. Ozansoy, and A. Ulhaq, "High-sensitivity vegetation high-impedance fault detection based on signal's high-frequency contents," *IEEE Trans. Power Del.*, vol. 33, no. 3, pp. 1398–1407, Jun. 2018.
- [7] W. H. Kwon, G. Lee, Y. M. Park, M. C. Yoon, and M. H. Yoo, "High impedance fault detection utilizing incremental variance of normalized even order harmonic power," *IEEE Trans. Power Del.*, vol. 6, no. 2, pp. 557–564, Apr. 1991.
- [8] B. D. Russell and C. L. Benner, "Arcing fault detection for distribution feeders: Security assessment in long term field trials," *IEEE Trans. Power Del.*, vol. 10, no. 2, pp. 676–683, Apr. 1995.
- [9] D. I. Jeerings and J. R. Linders, "Unique aspects of distribution system harmonics due to high impedance ground faults," *IEEE Trans. Power Del.*, vol. 5, no. 2, pp. 1086–1094, Apr. 1990.
- [10] J. R. Macedo *et al.*, "Proposition of an interharmonic-based methodology for high-impedance fault detection in distribution systems," *IET Gener. Transmiss. Distrib.*, vol. 9, no. 16, pp. 2593–2601, 2015.
- [11] T. Cui, X. Dong, Z. Bo, and A. Juszczak, "Hilbert-transform-based transient/intermittent earth fault detection in noneffectively grounded distribution systems," *IEEE Trans. Power Del.*, vol. 26, no. 1, pp. 143–151, Jan. 2011.
- [12] C.-H. Kim, H. Kim, Y.-H. Ko, S.-H. Byun, R. K. Aggarwal, and A. T. Johns, "A novel fault-detection technique of high-impedance arcing faults in transmission lines using the wavelet transform," *IEEE Trans. Power Del.*, vol. 17, no. 4, pp. 921–929, Oct. 2002.
- [13] W. C. Santos, F. V. Lopes, N. S. D. Brito, and B. A. Souza, "High-impedance fault identification on distribution networks," *IEEE Trans. Power Del.*, vol. 32, no. 1, pp. 23–32, Feb. 2017.
- [14] A. Ghaderi, H. A. Mohammadpour, H. L. Ginn, and Y. J. Shin, "High-impedance fault detection in the distribution network using the time-frequency-based algorithm," *IEEE Trans. Power Del.*, vol. 30, no. 3, pp. 1260–1268, Jun. 2015.
- [15] Y. Sheng and S. M. Rovnyak, "Decision tree-based methodology for high impedance fault detection," *IEEE Trans. Power Del.*, vol. 19, no. 2, pp. 533–536, Apr. 2004.
- [16] D. B. Russell, "Expert system for detecting high impedance faults," U.S. Patent 5 550 751, Aug. 27, 1996.
- [17] M. Michalik, M. Lukowicz, W. Rebizant, S. Lee, and S. Kang, "New ANN-based algorithms for detecting HIFs in multigrounded MV networks," *IEEE Trans. Power Del.*, vol. 23, no. 1, pp. 58–66, Jan. 2008.
- [18] P. H. Schavemaker and L. van der Sluij, "An improved Mayr-type arc model based on current-zero measurements [circuit breakers]," *IEEE Trans. Power Del.*, vol. 15, no. 2, pp. 580–584, Apr. 2000.
- [19] J. Schwarz, "Dynamisches Verhalten eines Gasbe-blasenen, Turbulenzbesetzten Schaltlichtbogens," *ETZ-A*, vol. 92, pp. 389–391, 1971.
- [20] V. Torres *et al.*, "Modeling and detection of high impedance faults," *Int. J. Electr. Power Energy Syst.*, vol. 61, pp. 163–172, 2014.
- [21] A. F. Sultan, G. W. Swift, and D. J. Fedirchuk, "Detecting arcing down-wires using fault current flicker and half-cycle asymmetry," *IEEE Trans. Power Del.*, vol. 9, no. 1, pp. 461–470, Jan. 1994.
- [22] P. Gopakumar *et al.*, "Remote monitoring system for real time detection and classification of transmission line faults in a power grid using PMU measurements," *Protection Control Modern Power Syst.*, vol. 3, no. 3, pp. 159–168, 2018.
- [23] W. Yu, W. Yao, and Y. Liu, "Definition of system angle reference for distribution level synchronized angle measurement applications," *IEEE Trans. Power Syst.*, vol. 34, no. 1, pp. 818–820, Jan. 2019.
- [24] A. Meier, E. Stewart, A. McEachern, M. Andersen, and L. Mehrmanesh, "Precision micro-synchrophasors for distribution systems: A summary of applications," *IEEE Trans. Smart Grid*, vol. 8, no. 6, pp. 2926–2936, Nov. 2017.
- [25] Z. Jin, H. Zhang, and C. Li, "WAMS light and its deployment in China," in *Proc. 5th Int. Conf. Elect. Utility Deregulation Restructuring Power Technol.*, Changsha, China, 2015, pp. 1373–1376.
- [26] A. M. Cassie, "Theorie Nouvelle des Arcs de Rupture et de la Rigidité des Circuits," CIGRE, Paris, France, Rep. 102, 1939.
- [27] O. Mayr, "Beiträge zur Theorie des statischen und des dynamischen Lichtbogens," *Archiv Für Elektrotechnik*, vol. 37, no. 12, pp. 588–608, 1943.
- [28] L. E. Fisher, "Resistance of low-voltage AC arcs," *IEEE Trans. Ind. Gen. Appl.*, vol. IGA-6, no. 6, pp. 607–616, Nov. 1970.
- [29] V. V. Terzija and H. J. Koglin, "Long arc in free air: Laboratory testing, modelling, simulation and model-parameters estimation," *IEE Proc.—Gener. Transmiss. Distrib.*, vol. 149, no. 3, pp. 319–325, May 2002.
- [30] D. B. Russell, M. B. Aucoin, and C. L. Benner, "Randomness fault detection system," U.S. Patent 5 485 093, Jan. 16, 1996.
- [31] D. B. Russell and M. B. Aucoin, "Energy analysis fault detection system," U.S. Patent 5 512 832, Apr. 30, 1996.
- [32] D. Hou, "Systems and methods for detecting high-impedance faults in a multi-grounded power distribution system," U.S. Patent 7 720 619, May 18, 2010.
- [33] R. F. Arritt and R. C. Dugan, "Distributed generation interconnection transformer and grounding selection," in *Proc. IEEE Power Energy Soc. Gen. Meeting-Convers. Del. Elect. Energy 21st Century*, 2008.
- [34] W. S. Moon, J. S. Hur, and J. C. Kim, "A protection of interconnection transformer for DG in Korea distribution power system," in *Proc. IEEE Power Energy Soc. Gen. Meeting*, 2012.
- [35] D. R. Christie, H. Zadehgol, and M. M. Habib, "High impedance fault detection in low voltage networks," *IEEE Trans. Power Del.*, vol. 8, no. 4, pp. 1829–1836, Oct. 1993.
- [36] D. L. Donoho, "De-noising by soft-thresholding," *IEEE Trans. Inf. Theory*, vol. 41, no. 3, pp. 613–627, May 1995.
- [37] M. U. Usman and M. O. Faruque, "Applications of synchrophasor technologies in power systems," *J. Mod. Power Syst. Clean Energy*, vol. 7, no. 2, pp. 211–226, Mar. 2019.
- [38] A. S. Karandaev *et al.*, "Information and measuring system for electric arc furnace transformer monitoring," in *Proc. 12th Int. Conf. Actual Probl. Electron. Instrum. Eng.*, 2014, pp. 273–279.
- [39] J. G. Mayordomo, L. F. Beites, R. Asensi, M. Izzeddine, L. Zubala, and J. Amantegui, "A new frequency domain arc furnace model for iterative harmonic analysis," *IEEE Trans. Power Del.*, vol. 12, no. 4, pp. 1771–1778, Oct. 1997.
- [40] C. J. Tennies and J. C. Zuercher, "Arc detection using current variation," U.S. Patent 5 561 605, Oct. 1, 1996.
- [41] D. B. Russell, M. B. Aucoin, and C. L. Benner, "Arc burst pattern analysis fault detection system," U.S. Patent 5 659 453, Aug. 19, 1997.



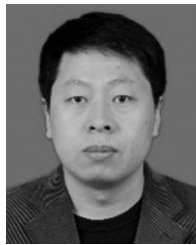
Mingjie Wei (S'17) received the B.S. degree in electrical engineering in 2017 from Shandong University, Jinan, China, where he is currently working toward the Ph.D. degree in electrical engineering with the Key Laboratory of Power System Intelligent Dispatch and Control of the Ministry of Education.

His research interest is mainly about the diagnosis of high impedance (arc) fault in the distribution system, including the techniques of model establishment, fault detection, and location.



Fang Shi received the B.E. degree in electrical engineering from the China University of Petroleum, Dongying, China, in 2006, the M.E. degree in electrical engineering from the State Grid Electric Power Research Institute, Nanjing, China, in 2009, and the Ph.D. degree from Shanghai Jiao Tong University, Shanghai, China, in 2014.

He is currently a Lecturer with the Key Laboratory of Power System Intelligent Dispatch and Control of the Ministry of Education, Shandong University, Jinan, China. His research interests include nonlinear control theory application in power systems, FACTS, and power system stability and control.



Hengxu Zhang (M'06) received the B.E. degree from the Shandong University of Technology, Zibo, China, in 1998, and the M.S. and Ph.D. degrees from Shandong University, Jinan, China, in 2000 and 2003, respectively, all in electrical engineering. He is currently a Professor with the Key Laboratory of Power System Intelligent Dispatch and Control of the Ministry of Education, Shandong University. His main research interests are power system security and stability assessment, power system monitoring, and numerical simulation.



Zongshuai Jin received the B.E. and Ph.D. degrees in electrical engineering from Shandong University, Jinan, China, in 2013 and 2019, respectively. His research interests include signal processing of power system, distribution-level synchrophasor measurement, high-precision identification of wideband signals of power systems, and synchronous data-driven situation awareness of smart grid.



Vladimir Terzija (M'95–SM'00–F'16) was born in Donji Baraci (former Yugoslavia). He received the Dipl.-Ing., M.Sc., and Ph.D. degrees in electrical engineering from the University of Belgrade, Belgrade, Serbia, in 1988, 1993, and 1997, respectively. He is currently the Engineering and Physical Science Research Council Chair Professor in Power System Engineering with the School of Electrical and Electronic Engineering, The University of Manchester, Manchester, U.K., where he has been since 2006. From 1997 to 1999, he was an Assistant Professor with the University of Belgrade. From 2000 to 2006, he was a Senior Specialist for switchgear and distribution automation with ABB AG, Inc., Ratingen, Germany. His current research interests include smart grid application of intelligent methods to power system monitoring, control, and protection; wide-area monitoring, protection, and control; switchgear and fast transient processes; and digital signal processing applications in power systems. He is the Editor-in-Chief for the *International Journal of Electrical Power and Energy Systems*, an Alexander von Humboldt Fellow, as well as a DAAD and Taishan Scholar.



Jian Zhou received the B.Sc. degree from the Department of Electrical Engineering, Shanghai Jiao Tong University, Shanghai, China, in 1997. He is currently the Director of the Power Grid Technology Center, State Grid Shanghai Municipal Electric Power Company, Electric Power Research Institute, Shanghai, China. He has authored/coauthored more than 25 journal and conference papers. His current research interests include smart distribution network technology and global energy Internet.



Hailong Bao received the master's degree from the Department of Electrical Engineering, Shanghai Jiao Tong University, Shanghai, China, in 2000. He is currently the Associate Director of Science and Technology Department, State Grid Shanghai Municipal Electric Power Company Electric Power Research Institute, Shanghai, China. He has authored/coauthored more than ten journal and conference papers. His current research interests include smart distribution network technology and smart grid.